Modeling and Control Experiments of a Fishtail-Like Pneumatic Soft Actuator

Kuo Xiong[1,2,3], Xuefeng Sun[1,2,3] and Qingxin Meng[1,2,3,*]

[1]*School of Automation, China University of Geosciences, Wuhan, Hubei 430074, China*

[2]*Hubei Key Laboratory of Advanced Control and Intelligent Automation for Complex Systems, Wuhan, Hubei 430074, China*

[3]*Engineering Research Center of Intelligent Technology for Geo-Exploration, Ministry of Education, Wuhan, Hubei 430074, China*

Abstract: As the exploration of deep-sea resources continues, underwater actuators with conventional motors as the main building blocks can no longer meet the increasingly demanding needs. Inspired by bionics, researchers have started to work on underwater actuators with bionic structures. In this study, we designed and implemented a novel Fishtail-like Pneumatic Soft Actuator (FPSA). This innovative actuator configuration is inspired by the tail structure of Body and/or Caudal Fin (BCF) mode fish. The actuator's motion is achieved by controlling the expansion and contraction of the pneumatic soft muscles on both sides. And by constructing an experimental platform, we conducted an in-depth performance characterization, revealing the existence of a frequency-dependent nonlinear hysteresis characteristic of the FPSA. In order to accurately characterize this property, we built a dynamic model of the FPSA and successfully identified the uncertain parameters in the model by applying the nonlinear least squares method. The validation results show that the constructed model can accurately describe the nonlinear hysteresis characteristics of the FPSA. Finally, we successfully realized the high-precision trajectory tracking control of the endpoint of the FPSA using a PID controller. This result provides relevant ideas for the research of novel underwater bionic actuators.

Keywords: Bionics, Pneumatic soft actuator, Nonlinear hysteresis, Dynamic modeling, Trajectory tracking control.

1. INTRODUCTION

Underwater vehicles play an important role in the field of ocean exploration and are capable of carrying out complex tasks such as seabed exploration, marine environmental monitoring and biological sampling in areas that are difficult for humans to reach [1]. These vehicles can collect data in real time and have good stability, providing strong support for scientific research and marine resources development [2]. With the development of science and technology, biomimicry, intelligence and high performance of underwater vehicles have become the focus of research [3]. However, in the process of performing tasks, the existing underwater vehicles still face many challenges such as excessive noise, insufficient maneuverability and weak environmental adaptability [4].

Conventional underwater vehicles mainly use electric motors as drive components, and although this drive method has been widely used, it still has many disadvantages that cannot be ignored [5]. First, propulsion devices composed of electric motors are usually large and inefficient, especially when low speed and fine control are required [6]. Secondly, motor drives generate a lot of noise when operating in the water, which not only destroys the living environment of underwater organisms, but also has an impact on the authenticity of data for marine life exploration. In

addition, traditional motor-driven underwater vehicles are also relatively weak in performing flexible motion and bionic propulsion, which makes it difficult to meet the needs of some special tasks [7].

In order to solve the above problems, more and more researchers have started to design more efficient, flexible and environmentally friendly underwater actuators based on biomimicry principles [8]. At present, some underwater actuators based on biomimicry principles have made some progress in research and design. For example, bionic fins [9], bionic wings [10], bionic flippers [11] and other actuators can mimic the way aquatic organisms swim in the water and provide more efficient and natural propulsion. However, most of the research on these bionic actuators is currently at the design stage, lacking in-depth analysis of the actuator performance, and the research on modeling and dynamic control of the actuators is still immature. Therefore, the research on how to accurately model, analyze the performance, and control these underwater bionic actuators with high precision has become an important issue that needs to be solved at present.

Against this background, this paper designs a fishtail-like pneumatic soft actuator (FPSA). The actuator draws on the movement of fish tail swing, adopts gas-driven technology, and simulates the natural movement of fish tail by controlling the airflow in order to regulate the tail swing and realize efficient underwater propulsion. On this basis, we also conducted an in-depth performance analysis, built a

*Address correspondence to this author at the School of Automation, China University of Geosciences, Wuhan, Hubei 430074, China;
E-mail: mengqx@cug.edu.cn

dynamic model of this fishtail-like pneumatic soft actuator to describe its motion characteristics, and realized high-precision trajectory tracking control of the FPSA end point through a PID controller.

2. PREPARATIONS

Body and/or Caudal Fin (BCF) mode fish mainly rely on the tail and caudal fins of the fish body to provide power for locomotion. In this section, we mimic the structure of BCF mode fish by designing a FPSA and build an experimental platform based on it for its control. Then, we collected preliminary data on the fishtail-like soft pneumatic robot and conducted a simple analysis of its characteristics.

2.1. FPSA Fabrication

In this subsection, we bionically designed the FPSA based on the body structure of BCF mode fish as shown in Figure **1**.

The tail of BCF mode fish is mainly divided into two sides of the muscle, the fish spine in the middle, and the caudal fin. Based on the above structure, our FPSA is mainly composed of pneumatic artificial muscle made of silicone material, bionic fishbone made of TPE material and bionic fish fin made of PLC material. Two pneumatic muscles are symmetrically pasted in the middle of the TPE bionic fish bone on both sides. The pneumatic muscles mimic the muscles of the fish's tail, which is the energy source for the robot's movement. The bionic fish bone mimics the backbone of a tuna, which is mainly used to support the pneumatic muscles of the robot. The bionic fins mimic the caudal fins of a fish, which generate a reaction force when they come into contact with water and serve as a source of power for the robot's movement.
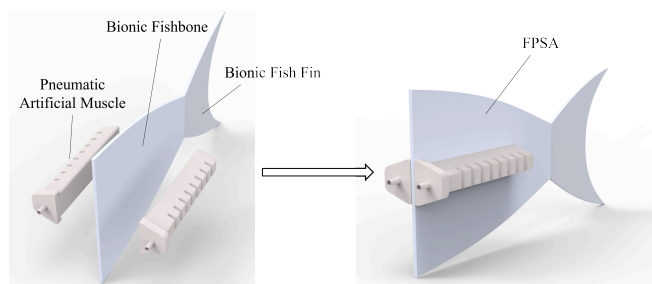

Figure 1: The structure of the FPSA.

The pneumatic artificial muscles utilized in this paper features an asymmetrical gas chamber design. Specifically, one side of it affixed to the TPE bionic fishbone has no airbags, while the other side boasts a row of them. Hence, when the internal air pressure of the artificial muscle is greater than the external atmospheric pressure, the side with the airbags expands, causing the artificial muscle to bend towards

the side without the airbags. Conversely, when the air pressure inside the actuator is less than the external atmospheric pressure, the side with the airbags contracts, thereby causing the artificial muscle to bend toward the side with the airbags. When alternately inflating and deflating the pneumatic artificial muscles on either side, the FPSA can achieve a swing back and forth like the BCF mode fish.

The artificial muscles on both sides of the FPSA are antagonistically structured. But the antagonistic driving structure design may lead to the cancellation of the driving effects of the two artificial muscles, resulting in waste of driving energy. To prevent such a situation and effectively utilize the movement characteristics of the pneumatic artificial muscle, we ensure that the control air pressure of one pneumatic artificial muscle is set as the opposite value to that of the other.

Next, we will develop an experimental platform for this FPSA, which will serve as a hardware foundation for the state measurement and control of the system.

2.2. FPSA Experimental Platform

Because the structure is similar to the BCF mode fish, the main factors affecting the magnitude of the propulsive force of the FPSA are the swinging amplitude and swinging frequency of the FPSA. In order to facilitate the state acquisition and control experiments of FPSA, we will build an experimental platform based on FPSA as shown in Figure **2**, which includes the following parts:

1. Computer (CPU: Intel i9-12900K, RAM: 32 GB), for calculating and sending control signals.

2. FPSA (Length: 300 mm, Height: 80 mm), and safe pressure range for the pneumatic soft actuators: -1~0.6 bar).

3. Proportional pressure control valve (Model number: VPPI-5L-3-G18-1V1H-V1-S1D, Festo, and output pressure range: -1~1 bar) for controlling the internal air pressure p of the FPSA.

4. Laser displacement sensor (Model number: IL-065, Keyence, and measuring range: 55~105 mm) for measuring the end-point displacement ω of the FPSA.

5. Input/Output (I/O) module (Model number: PCIe-6363, National Instruments) used as a channel for information transfer between the computer and the actual system.

6. Voltage source (Output range: 0~48V) for providing a stable DC voltage for experiments.

7. Positive pressure air pump (Model number: OTX-550X3, Outstanding, Volume: 65 L), for providing a stable source of positive air pressure to the experimental platform.

8. Negative pressure air pump (Model number: JBL-750, Jiabaoli, Volume: 36 L) for providing a stable source of negative air pressure to the experimental platform.
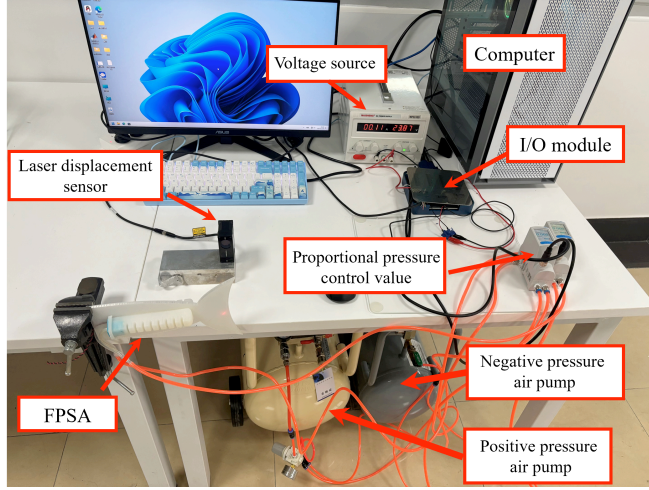

Figure 2: FPSA Experimental Platform.

2.3. Motion Characteristics Analysis

The FPSA is mainly made of silicone and TPE materials. Silicone and TPE are both flexible materials, and flexible materials usually exhibit complex properties, which can bring challenges to the modeling and control of the FPSA.

In order to accurately model and control the FPSA, we conducted open-loop experiments to collect data and do a preliminary motion characterization of the FPSA. Given the input air pressure of the FPSA according to (1) and making the frequency equal to 0.25 Hz, 0.5 Hz, 0.75 Hz, 1.0 Hz, 1.25 Hz, 1.5 Hz, respectively, we can obtain the endpoint displacement ω of the FPSA under variable input air pressure at different frequencies. The relationship between input air pressure and output displacement is shown in Figure **3**.

$$\begin{cases} t_m = rem(t, 6/f) \\ p_j(t_m) = a_j \sin\left(2f\pi\left(t_m - j/f\right)\right), j/f \le t_m \le \left(j+1\right)/f \end{cases}$$

(1)

where $j = 0, 1, 2, 3$, f is the frequency of the input air pressure, t is the time and p is the internal pressure of the FPSA; a_j is the amplitude of the j th wave, specifically $a_j = 0.3 + 0.1j$ bar.

From Figure **3**, we can find that the FPSA does not present a corresponding linear relationship between its input and output but is characterized by a highly nonlinear hysteresis. This characteristic makes the output value of the system at any moment not only related to the value of the input signal at the current moment, but also depends on the input value of the system at previous moments. The system representation exhibits memorability. In addition to that, this nonlinear hysteresis characteristic also has frequency-dependent property. We can find that the hysteresis loop size is different at different frequencies, and as the frequency increases, the hysteresis relationship between the input air pressure and output displacement becomes more obvious.

These complex kinematic characteristics will bring formidable difficulties to the characterization and control of the FPSA, so in the next section, we will build a model to further investigate the complex characteristics of the FPSA.

3. DYNAMIC MODELING
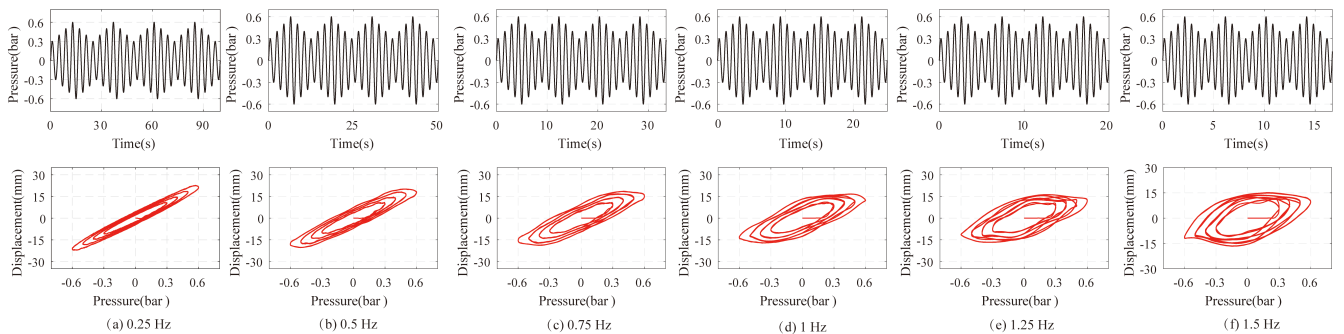
In the previous section, we found that FPSA has a

Figure 3: Motion characterization of the FPSA (In this figure, the solid black line represents the input air pressure, the solid red line represents the relationship between the input air pressure and the output displacement of the FPSA).

nonlinear hysteresis characteristic and that this characteristic is frequency-dependent. In order to accurately describe this complex characteristic of the FPSA, we established a dynamic model of the FPSA. Then the uncertain parameters in the model are identified by nonlinear least squares and the accuracy and generalization ability of the developed model is verified by validation set data.

3.1. Dynamic Modelling of the FPSA

One of the most common methods for modeling the nonlinear characteristics of pneumatic soft actuators is to use the image-only hysteresis model. The image-only hysteresis model starts from the image-only properties of the hysteresis curve and directly characterizes the hysteresis curve using an effective mathematical model without focusing on the physical meaning of the hysteresis system. Based on the image-only hysteresis model, the dynamic model we established contains two parts: the first part of the Prandtl-Ishlinskii (P-I) model, the second part of the transfer function, and its structure is as follows in Figure **4**.
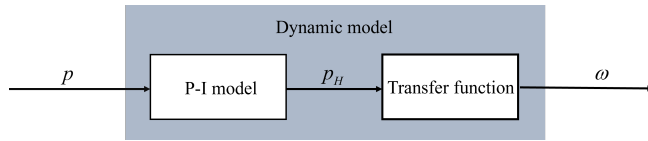

Figure 4: The structure of dynamic models.

(1). P-I Model

The P-I model can describe the nonlinear hysteresis characteristics of the system with fewer parameters, the model error is not cumulative, and its analytic inverse is easy to derive. Due to the symmetry of the basic hysteresis operator of the P-I model, the P-I model is often used to describe the symmetrical hysteresis of the system.

According to the above Figure **3**, it can be found that the hysteresis loop of the system is counterclockwise and roughly symmetric, so we use the P-I model to characterize the hysteresis of the system, and adopt the Play operator as the basic hysteresis operator of the P-I model. The Play operator $H_{r_i}[p](k)$ is defined as follows,

$$\begin{cases} H_{r_i}[p](0) = h_{r_i}\left(p(0),0\right) \\ H_{r_i}[p](k) = h_{r_i}\left(p(k),H_{r_i}[p](k-1)\right) \end{cases} \quad (2)$$

where $h_{r_i}(p,v) = \max(p-r_i,\min(p+r_i,v))$, k is the k th sampling time, r_i is the threshold value of the Play

operator, which is usually selected according to the amplitude of the input signal. In this paper, the size of r_i is: $r_i = \dfrac{i-1}{N-1}\max\left\{|P|\right\}, i = 1,2,\cdots,N$, N is the number of Play operators, P is the set of all time p.

Based on the above Play operator, the output $p_H(k)$ of the P-I model is defined as,

$$p_H(k) = \sum_{i=1}^{N} c_i H_{r_i}[p](k) \quad (3)$$

where c_i is the weight of the i th Play operator.

(2). The Transfer Function

According to Figure **3** above, it can be found that the hysteresis of the FPSA has rate-dependent characteristics, *i.e.*, the hysteresis characteristics of the FPSA are various at different frequencies. While a single P-I model only describes the frequency-independent hysteresis characteristics, we string a transfer function based on the above P-I model to describe the frequency-dependent hysteresis characteristics. The transfer function can be expressed as

$$G(s) = \frac{S^{m_L} + b_{m_L-1}s^{m_L-1} + \ldots + b_1 s + b_0}{S^{n_L} + a_{n_L-1}s^{n_L-1} + a_{n_L-2}s^{n_L-2} + \ldots + b_1 s + b_0} \quad (4)$$

where a_i and b_i are undetermined constants; s is Laplace operator; m_L and n_L are positive constants, $m_L < n_L$.

In this paper, we use a second-order transfer function to describe the frequency-dependent characteristics, which can be represented as

$$\begin{cases} \dot{x}_1 = x_2 \\ \dot{x}_2 = \dfrac{-a_1 x_2 - a_0 x_1 + b_0 p_H}{a_2} \end{cases} \quad (5)$$

where x_1 represents the endpoint displacement ω of the FPSA, x_2 represents the velocity; a_2, a_1, a_0, and b_0 are all unknown parameters.

3.2. Parameter Identification

The dynamic model developed above contains unknown parameters c_i, a_2, a_1, a_0, and b_0. These parameters need to be identified by collecting a large amount of experimental data and utilizing intelligent algorithms for parameter identification.

We use nonlinear least squares to identify the unknown parameters in the model in this paper. The nonlinear least squares method finds the optimal parameter X by finding the parameter that minimizes the cost function $E(X)$ among different parameters.

$$E(X) = \sum_{i=0}^{m} e_i^2 = \sum_{i=0}^{m} \left[\omega_{mi}(X) - \omega_i\right]^2 \qquad (6)$$

where m is the total length of the data, X is the unknown parameter vector, $X = [x_1, x_2, \cdots, x_r]$, r is the number of unknown parameters; ω_i is the i th actual data, $\omega_{mi}(X)$ is the i th predicted value under the estimated parameter vector of X.

Here we use the LM iterative algorithm to perform nonlinear least squares identification of the unknown parameters. Its main steps are as follows:

1) Define the cost function, *i.e.*, $E(X)$

2) Initialize the estimated parameter vector X, usually with random or empirical values.

3) Compute the Jacobian matrix J of the valence function $E(x)$ with respect to the estimated parameter vector X.

4) Calculate the value of the initial cost function by substituting the initial estimated parameters X.

5) Set the parameters of the LM algorithm, including the initial damping factor λ, the maximum number of iterations, the iteration accuracy, the convergence step, etc.

6) Update the parameter vector by iteration with the update criterion $X = X + \Delta X$, $\Delta X = \left(J^T J + \lambda I\right)^{-1} J^T \left[\omega - \omega_m(X)\right]$. And use the new estimated parameter to substitute into the cost function $E(X)$, calculate whether the new cost function is smaller or not, if it is smaller then accept the updated estimated parameter X,

otherwise reject the update and increase $\lambda = 10\lambda$, and if the new parameter is better then decrease $\lambda = 0.1\lambda$.

7) After updating the estimated parameters, repeat step 6) continuously. If the change in the value of the cost function is less than the set iteration accuracy, or the maximum number of iterations is reached, the iteration is stopped and the optimal parameter vector X is returned.

Further, the root-mean-square error percentage e_{rmsp} in (7) and the maximum error e_{mp} in (8) are defined to verify the accuracy of the parameter identification results.

$$e_{rmsp} = \frac{\sqrt{\dfrac{1}{N}\sum_{i=1}^{N}(\omega_{mi} - \omega_i)^2}}{\max(\omega_i) - \min(\omega_i)} \times 100\% \qquad (7)$$

$$e_{mp} = \frac{\max(\omega_{mi} - \omega_i)}{\max(\omega_i) - \min(\omega_i)} \times 100\% \qquad (8)$$

where ω_{mi} is the output predicted by the model at the i th sampling point and ω_i is the actual FPSA output at the i th sampling point.

By using the above nonlinear least squares method for the identification of unknown parameters in the model, we identify the parameter results as in Table **1** and the identification effect as in Figure **5**. As can be seen from Figure **5**, the fitting effect of this model is very good, and its fitting accuracy is a little better in the low frequency range and a little lower in the high frequency range. This is due to the limitation of the hardware equipment, in the process of data acquisition, when the frequency of the input gas pressure is more than 1Hz, the filling and deflating speed inside the FPSA is too fast, which exceeds the maximum gas flow rate that can be controlled by the proportional valve of the gas pressure. This leads to a certain saturation effect when the data exceeds 1Hz, which is ignored during the modeling of this experiment. Although the
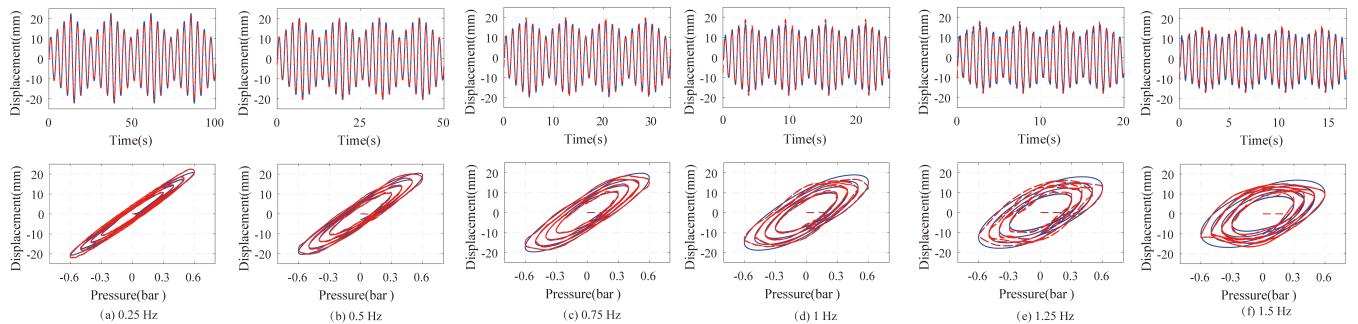

Figure 5: The identification results (In this figure, the solid red line represents the experimental data, and the dashed blue line represents the model output. The top half of each subplot is a comparison of the recognition results for the output displacement, and the bottom half is a comparison of the recognition results for the hysteresis loop).

Table 1: The Parameter Rersults

Unknown Parameters	Identification Results	Unknown Parameters	Identification Results
c_1	992.48	c_8	71.84
c_2	560.65	c_9	33.05
c_3	-347.35	c_{10}	71.23
c_4	-27.09	b_0	5.92
c_5	-58.19	a_0	0.59
c_6	83.87	a_1	22.18
c_7	89.80	a_2	205.21

fitting accuracy is slightly lower for data above 1Hz, the error is still within acceptable limits. The E_{rmsp} between the predicted output of the model and the actual output of the system is 2.28%. The results show that the identified model parameters can well describe the nonlinear hysteresis characteristics of FPSA. Therefore, the model is suitable for the study of the FPSA.

3.3. Validation of Model Parameters

To further illustrate the accuracy and generalization ability of the model based on the parameters identified above, two validation datasets were collected with variable inputs at different frequencies.
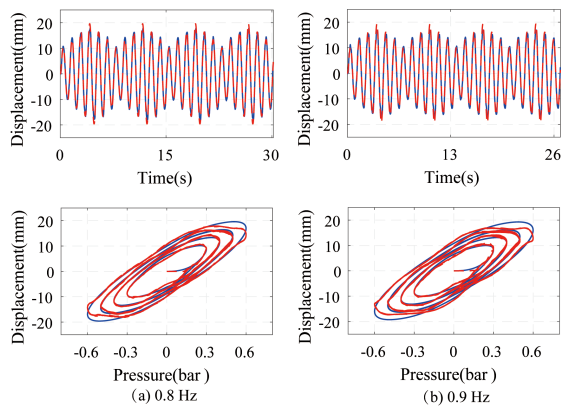

Figure 6: Model validation results

Figure **6** shows the comparison between the actual data of the validation set and the prediction results of the validation set inputs under the model. We can find that under the verification set of 0.8 Hz and 0.9 Hz, E_{rmsp} is 2.07% and 2.56% respectively, then E_{mp} is 8.09% and 9.75% respectively, which also has good prediction accuracy. It shows that the dynamic model based on the above parameters can accurately describe the dynamic characteristics of the FPSA.

4. CONTROLLER EXPERIMENT

As described in the foregoing text, FPSA possesses complex nonlinear hysteresis characteristics. Therefore, it is challenging to directly control the end point of FPSA to swing along the target trajectory. In this section, we propose to utilize a PID controller to implement trajectory tracking control of the end point of FPSA and validate the feasibility of this strategy through a series of experiments.

4.1. PID Controller

PID controller is a widely used feedback control mechanism that adjusts the control input based on the error between the desired and actual positions or states. The PID controller combines three control actions:

1)   Proportional control (P): This term provides an output that is proportional to the current error. The proportional gain determines how much the control output will be influenced by the magnitude of the error.

2)   Integral control (I): This term accounts for the accumulation of past errors. It is used to eliminate steady-state error by adjusting the control output based on the sum of past errors over time.

3)   Derivative control (D): This term predicts future error by computing the rate of change of the error. It helps to reduce overshoot and improve system stability by counteracting the effects of rapid error changes.

The combined action of these three terms provides a control output that minimizes the error and achieves the desired system behavior.

The control output $u(t)$ of a PID controller is given by the following equation:

$$u(t) = K_P e(t) + K_i \int_0^t e(\tau)\,d\tau + K_d \frac{de(t)}{dt} \qquad (9)$$

where $e(t)$ is the trajectory tracking error at time t. K_p is the proportional gain, which controls the response to the current error. K_i is the integral gain, which controls the response to the accumulated error over time. K_d is the derivative gain, which controls the response to the rate of change of the error.

By adjusting the gains K_p, K_i and K_d, the PID controller can be tuned to achieve optimal performance in various dynamic systems, including trajectory tracking in complex systems like the FPSA. Based on the above PID controller, we designed the controller structure shown in Figure **7** for the FPSA to achieve high-precision trajectory tracking control of the endpoint of the FPSA.
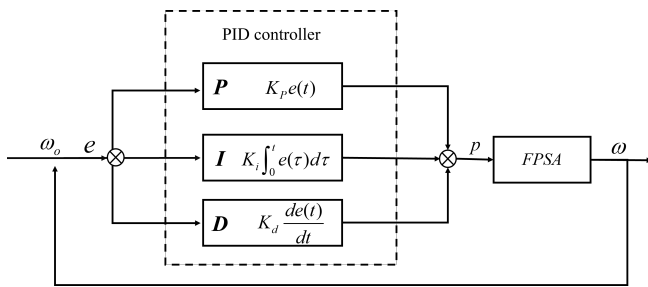
Figure 7: The Controller structure of the FPSA.

4.2. Trajectory Tracking Control Experiment

In this section we will use three sets of tracking control experiments with different trajectories to verify the finiteness and generalization ability of the proposed control strategy. Through continuous trial and error tuning, the optimal parameters of the PID controller were determined to be $K_p = 0.0004$, $K_i = 0.5$ and $K_d = 0.0002$.
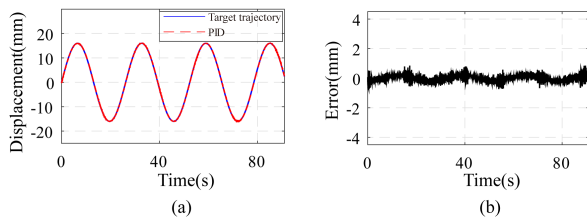
Figure 8: Experimental results of tracking control for sinusoidal wave trajectories.

The first target trajectory was set as a simple sinusoidal wave with an amplitude of $a = 6$ mm and a frequency of $f = 0.04$ Hz, and the results are shown in Figure **8**. And Figure **8**(**a**) compares the tracking

performance with the reference trajectory, while Figure **8**(**b**) shows the tracking error. After processing and analyzing the data, it was found that the error during sinusoidal trajectory tracking remains within an acceptable range, with the E_{rmsp} is 0.61% and the E_{mp} is 2.65%.

The second target trajectory was set as a triangular wave with an amplitude of $a = 8$ mm and a period of 20 seconds. The corresponding verification results are shown in Figure **9**. Data analysis reveals that, compared to the sinusoidal trajectory tracking experiment, the error of the triangular wave trajectory tracking is slightly higher but still within an acceptable range, with the E_{rmsp} is 0.99% and the E_{mp} is 5.53 %.
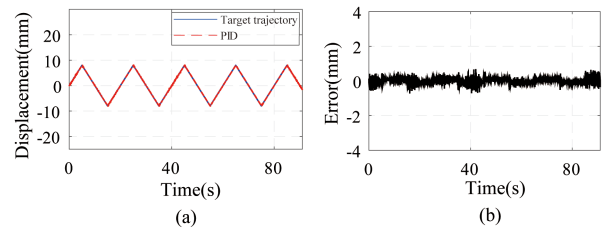
Figure 9: Experimental results of tracking control of triangular wave trajectories.

The third target trajectory was designed as a sinusoidal wave with varying amplitude and frequency, with amplitudes $a_1 = 4$ mm, $a_2 = 6$ mm, $a_3 = 8$ mm, $a_4 = 10$ mm, $a_5 = 12$ mm and corresponding frequencies $f_1 = 0.1$ Hz, $f_2 = 0.2$ Hz, $f_3 = 0.3$ Hz, $f_4 = 0.4$ Hz, $f_5 = 0.5$ Hz. The results for this test are presented in Figure **10**. After analyzing the data, it is evident that the error for the varying amplitude and frequency sinusoidal trajectory tracking is larger than the errors observed in the previous two tracking experiments. This is because the target trajectory set in the variable frequency experiment is not a smooth trajectory, and the point at the moment of frequency switching is a non-smooth point, which makes the PID controller jitter, and makes the control effect worse. In addition, the traditional PID controller has the limitation that a fixed set of controller parameters cannot perform well in all frequency bands when the target trajectory frequency span is large. New control methods need to be explored subsequently to address this point in the future. However, it can be found through Figure **10** that the control effect of the variable frequency experiment is still relatively favorable, with the E_{rmsp} is 2.5282% and the E_{mp} is 10.48%. These errors are still within an acceptable range.

Through three sets of tracking experiments with different trajectories, it can be found that the proposed control strategy has good tracking accuracy for sinusoidal waves, triangular waves, and complex waves whose frequency and amplitude are changed. This fully demonstrates the feasibility of using PID

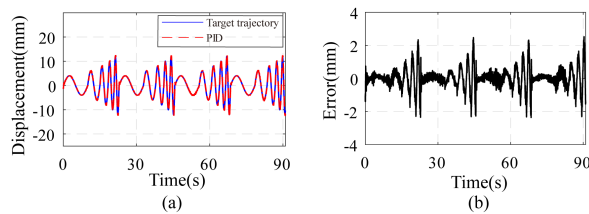controllers to realize the precise control of the endpoint of the FPSA.

Figure 10: Experimental results of tracking control for complex wave trajectories.

5. CONCLUSION

In this study, we design and implement a new driver propulsion device, the FPSA, by borrowing the tail structure of the BCF mode fish. We construct an experimental platform for the FPSA and conduct an in-depth analysis of its performance characteristics. Through this series of characterization, we found that the FPSA exhibits a nonlinear hysteresis characteristic related to the frequency of the input signal.

In order to provide a more accurate characterization of this property, we design and build a dynamic model of the FPSA. By applying the nonlinear least squares method, we successfully identify the uncertain parameters in the model. It is verified that the constructed model can accurately describe and predict this nonlinear hysteresis property of the FPSA with respect to the frequency of the input signal.

In the final stage of our research, we realized the high precision trajectory tracking control of the FPSA endpoint using a PID controller. This result provides a strong empirical support for our study and a valuable reference for future related research.

ACKNOWLEDGMENT

CONFLICTS OF INTEREST

No potential conflict of interest was reported by the author(s).

REFERENCES

[1] Zhang, Bingbing, *et al*. "Autonomous underwater vehicle navigation: a review." Ocean Engineering 273 (2023): 113861.
https://doi.org/10.1016/j.oceaneng.2023.113861

[2] Bao, Haimo, *et al*. "A review of underwater vehicle motion stability." Ocean Engineering 287 (2023): 115735.
https://doi.org/10.1016/j.oceaneng.2023.115735

[3] Wibisono, Arif, *et al*. "A survey on unmanned underwater vehicles: Challenges, enabling technologies, and future research directions." Sensors 23.17 (2023): 7321.
https://doi.org/10.3390/s23177321

[4] Ahmed, Faheem, *et al*. "Survey on traditional and AI based estimation techniques for hydrodynamic coefficients of autonomous underwater vehicle." Ocean Engineering 268 (2023): 113300.
https://doi.org/10.1016/j.oceaneng.2022.113300

[5] Chen, Gang, *et al*. "Swimming modeling and performance optimization of a fish-inspired underwater vehicle (FIUV)." Ocean Engineering 271 (2023): 113748.
https://doi.org/10.1016/j.oceaneng.2023.113748

[6] Li, Zhihan, *et al*. "Development of a multi-tentacled collaborative underwater robot with adjustable roll angle for each tentacle." Ocean Engineering 308 (2024): 118376.
https://doi.org/10.1016/j.oceaneng.2024.118376

[7] Fu, Jian, *et al*. "A unified switching dynamic modeling of multi-mode underwater vehicle." Ocean Engineering 278 (2023): 114359.
https://doi.org/10.1016/j.oceaneng.2023.114359

[8] Cui, Zhongao, *et al*. "Review of research and control technology of underwater bionic robots." Intelligent Marine Technology and Systems 1.1 (2023): 7.
https://doi.org/10.1007/s44295-023-00010-3

[9] Chen, Long, *et al*. "Research on underwater motion modeling and closed-loop control of bionic undulating fin robot." Ocean Engineering 299 (2024): 117400.
https://doi.org/10.1016/j.oceaneng.2024.117400

[10] Ge, Liming, *et al*. "Design and analysis of wire-driven tail fin for bionic underwater glider." Ocean Engineering 286 (2023): 115460.
https://doi.org/10.1016/j.oceaneng.2023.115460

[11] Li, Hanlin. "Bionic, Fin-propelled Underwater Multi-legged Robot." 2023 IEEE 3rd International Conference on Power, Electronics and Computer Applications (ICPECA). IEEE, 2023.
https://doi.org/10.1109/ICPECA56706.2023.10075778